Refinement of the upper limb joint kinematics and dynamics using a subject-specific closed-loop forearm model

Maria Laitenberger · Maxime Raison · Delphine Périé · Mickael Begon

Abstract A biofidelic multibody model of the upper limb for the quantitative assessment of joint kinematics and dynamics has the potential to become an innovative tool in many application fields. However, forearm kinematic modeling still presents challenges due to the complexity of providing a closed-loop and subject-specific definition of its multiple degrees of freedom. In this context, this study aims to refine the upper limb multibody model by means of a forearm closed-loop kinematic chain and personalized joint parameters to quantify the forearm joint kinematics and dynamics. To assess the benefits of this refinement, the proposed model is compared to four conventional models according to (i) the global and local movement reconstruction errors during inverse kinematics and (ii) the joint torque-angle pattern. Fifteen (15) healthy adults performed two cyclic dynamic tasks, namely elbow flexion–extension (FE) and forearm pronation–supination (PS). Results show that the proposed model leads to a reduction of the global reconstruction error up to 15 % and 31 % during FE and PS tasks, respectively, while computational times remain similar. The local reconstruction errors show less compensation at the shoulder and wrist for the proposed model. The PS angle and torque are increased by 24 % during the PS task for the proposed model when compared to conventional models. In conclusion, this study addresses novel methodology aspects and a comprehensive description of a forearm multibody model that can serve in multiple applications requiring a realistic representation of the upper limb kinematics and dynamics without increasing the computational time.

M. Raison (✉)
Research & Engineering Chair Applied in Pediatrics (RECAP), CRME—Sainte-Justine UHC,
5200 rue Bélanger, office GR-123, Montreal, Qc, Canada H1T 1C9
e-mail: maxime.raison@polymtl.ca

M. Laitenberger · M. Raison · D. Périé
Department of Mechanical Engineering, École Polytechnique de Montréal, Montreal, Qc, Canada

M. Laitenberger · D. Périé
Research Center, Sainte-Justine UHC, Montreal, Qc, Canada

M. Begon
Department of Kinesiology, Université de Montréal, Montreal, Qc, Canada

Keywords Inverse kinematic and dynamic analysis · Global optimization · Closed-loop multibody systems · Subject-specific modeling · Upper limb · Forearm

Abbreviations

3D	three-dimensional
AC	acromioclavicular
AoR(s)	axis (axes) of rotation
BSIP	body segment inertia parameters
CoR(s)	center(s) of rotation
DoF(s)	degree(s) of freedom
FE	flexion–extension
GH	glenohumeral
GO	global optimization
HR	humeroradial
HU	humeroulnar
ISB	International Society of Biomechanics
LCS	local coordinate system
MRI	magnetic resonance imaging
PS	pronation–supination
RC	radiocarpal
RU	radioulnar
SARA	symmetrical axis of rotation approach
SC	sternoclavicular
SCoRE	symmetrical center of rotation estimation

1 Introduction

Following the increasing interest in upper extremity biomechanics, advanced biomechanical methods have been combined with multibody modeling to provide a biofidelic representation of the upper limb osteoarticular system [1–8]. Many application fields such as comfort analysis of car occupants [9], sport performance analysis [10] or impact analysis in swing-through crutch gait [11] could benefit from a refined quantitative assessment of joint kinematics and dynamics of the upper limb. In rehabilitation, it may be clinically helpful to evaluate the outcome of a treatment in post-stroke robot-assisted training [12], to detect pathological movement patterns during manual wheelchair propulsion [13], to develop neuroprosthetic systems [14], as well as to evaluate functional capacity in hemiparetic patients [15].

Nevertheless, several aspects need to be investigated before such a tool can become routinely used in biomedical applications. One of the key features in obtaining clinically exploitable results is patient-specific modeling [16]. In the design of any biomechanical model, a certain level of sophistication is also mandatory to provide a realistic representation of human motion. This can be achieved by a kinematic refinement since joint angles and torques are not only affected by the model inputs but also by the choice of an appropriate kinematic model, i.e., a particular sequence of degrees of freedom (DoFs) that describes the relative motions allowed by each joint, and by the joint parameters describing the relative pose (position and orientation) for each of these DoFs. Many three-dimensional (3D) kinematic models of the upper extremity have focused on the refinement of shoulder kinematics [17–19] while the refinement of the forearm model still presents some modeling challenges due to the complexity of its multiple DoFs arranged in a closed-loop kinematic chain [2, 20, 21].

In this context, this paper aims to present the development of an upper limb multibody model that uses a forearm closed-loop kinematic chain and subject-specific information. To expose the effect of the level of refinement in the forearm multibody modeling and its relevance in upper limb joint kinematics and dynamics, the proposed model is then compared to four conventional models that support the main assumptions of the literature, as described in the following survey of the state-of-the-art. The comparison is based on (i) the global and local movement reconstruction errors during inverse kinematics and (ii) the joint torque-angle patterns. It is expected that the increase in the level of refinement will reduce the movement reconstruction errors and lead to a different torque-angle pattern. The incentive behind this work is to develop a robust multibody model of the upper limb that can be used for clinical applications.

2 Forearm biomechanics: state-of-the-art

In the literature, there is still a need for a clear description of the mechanisms underlying the forearm functional movements namely elbow flexion–extension (FE) and particularly elbow pronation–supination (PS) which is at an early stage of development. This section presents a survey of the state-of-the-art to highlight the current limitations regarding the kinematic modeling of these two movements.

In regard to the elbow joint, the FE movement is guided by the ulna trochlear notch, which rotates along the humerus trochlea. This DoF is commonly modeled as a unique revolute joint. When modeling the elbow complex osteoarticular structure, earlier attempts were restricted to a cardanic joint successively describing the FE and PS DoFs [22]. However, based upon a cadaveric study, Veeger et al. [23] highlighted the fact that the FE and PS axes are not perpendicular. The physiological valgus of the forearm regarding the humerus, i.e., the relative acute angle between the humerus longitudinal axis and the forearm longitudinal axis, is also known as the carrying angle (Fig. 1(a)). It is recognized that the natural carrying angle is around 14° in women and 11° in men [24]. However, this angle is known to be subject-specific [25] and must therefore be considered when undertaking biofidelic osteoarticular modeling. To take this angle into account, a few authors introduced a fixed angle value in the reference configuration [5, 8] while others suggested that this angle varies linearly to FE [26–28]. Many recent studies have modeled the elbow kinematic joint by a spherical joint, considering the carrying angle around the floating axis between the FE and PS angles [4, 27, 29]. Ultimately, there is no consensus on how to replicate the physiologically observed carrying angle in the forearm multibody model. Its definition may substantially influence the joint kinematics and dynamics of the upper limb.

Besides, the forearm PS movement can be seen as a closed 3D mechanism with the two forearm bones, the ulna and radius, linked at their ends by the elbow and the wrist joints. During the PS movement, this intricate 3D four-bar linkage allows the radius to turn around the ulna while the hand remains aligned with the forearm axis (Fig. 1(b)). Only a few studies have attempted to improve the definition of the forearm kinematic chain during the PS movement [2, 20, 30], especially concerning the proximal and distal radioulnar joints. Early studies such as Lemay and Crago [31] described the relative motion between the two forearm bones under the assumption that the ulna is fixed with respect to the humerus, which led to an unrealistic tilt of the wrist [2].

Thanks to magnetic resonance imaging (MRI) studies [32, 33], it was demonstrated that rotation (tilting) and translation (dislocation) of the ulna with respect to the humerus occur during the PS movement. Thus, the PS joint is not an ideal revolute joint, contrary to what

Fig. 1 (**a**) Representation of the carrying angle, i.e., the relative acute angle between the humerus longitudinal axis and the forearm longitudinal axis.
(**b**) Representation of the pronation–supination movement
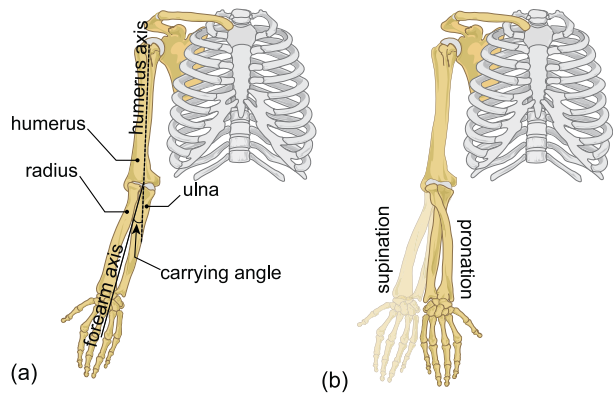
conventional models may assume. To consider this non-ideal behavior, Kecskeméthy and Weinberg [2] developed a closed-loop surrogate mechanism that was validated using an MRI-based automatic procedure [21], establishing it as one of the most comprehensive PS models. Concerning its closed kinematic chain, this kinetostatic model originally introduced torsional and aperture angles between the radius and ulna. The authors also integrated axial displacement and lateral swaying of the ulna with respect to the humerus, which had been neglected until then. Although this model has been recognized for its ability to reproduce the static behavior of the forearm, it was developed for a fixed elbow FE position. Thus, this model has not been integrated into a complete upper limb model or used in dynamic condition.

Despite the fact that Kecskeméthy and Weinberg [2] had brought a closer investigation to the complex nature of the forearm osteoarticular structure, most of the recently published forearm models still present important limitations. There is often no interaction between the radius and the ulna as observed in the anatomy, since the forearm is mostly represented as a unique segment [7, 22, 27, 29]. Moreover, the forearm PS movement is often expressed through DoFs at the elbow only, and not by considering a coupling between the proximal and distal radioulnar joints. More recently, Pennestrì et al. [3] have made a distinction between the two forearm bones by adding revolute guide and universal joints at the wrist. However, their model neglected the lateral swaying and axial sliding of the ulna at the humeroulnar joint. Hence, a large proportion of the dynamic models of the upper extremity are still hindered by a kinematic model that oversimplifies the DoFs involved during the PS movement—a movement that is crucial to the functioning of the upper limb in everyday tasks [4, 34].

The International Society of Biomechanics (ISB) [35] has recommended the use of standardized local coordinate systems (LCS). The description of the upper limb joint kinematics is based on anatomical landmarks associated to each bony segment. Since these anatomical LCS are only a first-order approximation of the real FE and PS axes of rotation, their use can result in a joint kinematics substantially affected by kinematic cross-talk [5, 6, 36]. The kinematic cross-talk is minimal when in a movement principally recruiting one DoF the amplitudes of the other DoFs of the same joint are minimal. To reduce this drawback, a few authors have personalized the joint parameters, i.e., joint centers (CoRs) and axes (AoRs) of rotation, at the upper limb by using in vivo functional methods [8, 18, 25, 37]. For instance, the recent model of Fohanno et al. [8] included personalized and non-intersecting forearm FE and PS axes by means of recognized in vivo functional methods, namely the symmetrical center of rotation estimation (SCoRE) [38] and the symmetrical axis of rotation approach

(SARA) [39, 40]. This personalization increased the relative contribution of the PS DoF by 15 % in terms of the total joint angle amplitudes in comparison to the ISB standard model. However, by modeling the forearm as one single rigid body, this study did not represent the interactions between the ulna and the radius. Furthermore, these functional methods had not been exploited for determining the CoRs in a complete closed-loop forearm model.

The above state-of-the-art survey shows that conventional forearm models are often represented as an open-chain system. However, to consider the two forearm bones as separate bodies and to be consistent with the functional anatomy of the forearm, a closed-loop kinematic model is required. Models that oversimplify the forearm multiple DoFs as well as their joint pose definitions limit their ability to reproduce the upper limb function and thus, their clinical applications. To obtain clinically exploitable results, the challenge is therefore to develop a subject-specific closed-loop forearm model.

3 Methods

This section first describes the proposed model and for comparison purposes, four commonly used models. Then, the processing method for kinematic data acquisition and inverse kinematic and dynamic analysis is presented. Finally, the comparative aspects that serve to assess the proposed model are detailed.

3.1 Proposed model

3.1.1 Kinematic chain

The proposed multibody model includes the thorax, clavicle, scapula, humerus, ulna, radius, and hand modeled as rigid bodies as described in Table 4 of Appendix A and depicted by Fig. 2. The thorax is defined as the moving base of the model with six DoFs (q_{1-6}). The sternoclavicular (SC), acromioclavicular (AC) and glenohumeral (GH) joints are defined as spherical joints (q_{7-9}, q_{10-12} and q_{13-15}, respectively). In agreement with the ISB recommendations [35], AC and SC joints are defined by a rotation Cardan angle sequence, successively representing the flexion–extension, abduction–adduction and external–internal rotation movements. The GH joint is defined using an Euler angle representation successively representing the plane of elevation, elevation, and axial rotation movements. Note that the shoulder girdle is a very complex structure [17–19] that can also be modeled as a closed-loop mechanism. However, in the present study focusing on the forearm where arm elevation above 120° is avoided, it is possible to neglect the scapulothoracic gliding plane and to model the shoulder using three successive spherical joints (SC, AC and GH) [6].

The proposed model integrates a revolute joint representing the elbow FE DoF (q_{16}) at the humeroulnar (HU) joint, followed by a closed-loop PS mechanism (q_{17-21}) [2]. The latter considers the specific DoFs associated with the forearm PS as well as the interactions between the ulna and the radius. More specifically, this model takes into account the evasive motion of the ulna and the carrying angle by means of both the axial displacement (q_{17}) and the swaying rotation (q_{18}) of the ulna with respect to the humerus at the HU joint. After the intrinsic PS angle (q_{19}), this model also includes the torsional (q_{20}) and aperture (q_{21}) angles between the ulna and the radius at the radioulnar (RU) joint and a virtual CoR, as proposed by Kecskeméthy and Weinberg [2]. The system is then closed by a cut of ball joint at the humeroradial (HR) joint, comprising three kinematic loop-closure constraints. Let us note that the forearm axis is defined between the HR and RU joints but is not in

Fig. 2 Kinematic chain of the proposed multibody model. The model is articulated by a moving base (q_{1-6}), the sternoclavicular joint (SC, q_{7-9}), the acromioclavicular joint (AC, q_{10-12}), the glenohumeral joint (GH, q_{13-15}), the humeroulnar joint (HU, q_{16-18}), the radioulnar joint (RU, q_{19-20}), the virtual CoR (q_{21}), the humeroradial joint (HR, cut of ball joint with three kinematic loop-closure constraints), and the radiocarpal joint (RC, q_{22-23}). See Table 4 of Appendix A for the detailed description of the kinematic chain
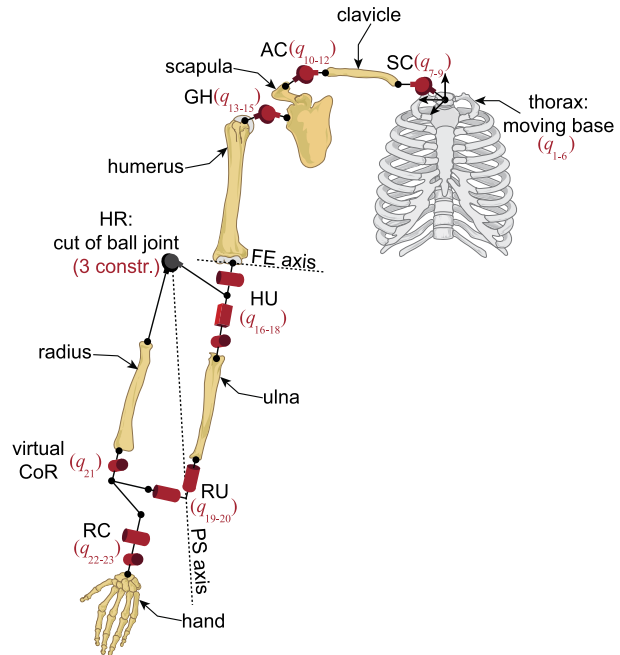
a fixed orientation during motion since this axis is a result of the multiple DoFs (q_{17-21}) comprising the closed-loop. Furthermore, unlike the theoretical kinetostatic model presented in [2] where it is assumed that the forearm mechanism lies flat and parallel in full supination, the proposed model is based on non-ideal assumptions using a functional subject-specific approach described in Sect. 3.1.2. Finally, the wrist joint is modeled using two DoFs as a universal joint at the radiocarpal (RC) joint, representing flexion–hyperextension (q_{22}) and ulnar–radial deviation (q_{23}) of the hand with respect to the radius.

3.1.2 Personalized joint centers and axis of rotation

A notable difference from the ISB recommendations and the theoretical model of Kecskeméthy and Weinberg [2] is that the link origin between each rigid body is defined in a functional manner to provide a subject-specific and optimal kinematic definition. Thus, the joint CoRs (SC, AC, GH, RU, HU, HR, RC) and the elbow FE AoR are personalized using the SCoRE and SARA functional methods [38–40] respectively.

3.1.3 Local coordinate systems

Technical local coordinate systems (LCS) are used to locate the CoRs and AoR. These technical LCS are built using all the markers on each segment, then optimized from a static configuration using the conjugate gradient algorithm to minimize soft tissue artefacts [41]. Based on the CoR and AoR locations, anatomical LCS according to the ISB recommendations [35] are then defined to describe the joint rotations of the thorax, clavicle, scapula, and hand. To describe the joint kinematics in a clinically meaningful manner at the forearm, two LCS are used for the humerus: one anatomical LCS provided by the ISB [35] at the proximal end to describe the GH joint rotations, and one functional LCS at the distal end to describe
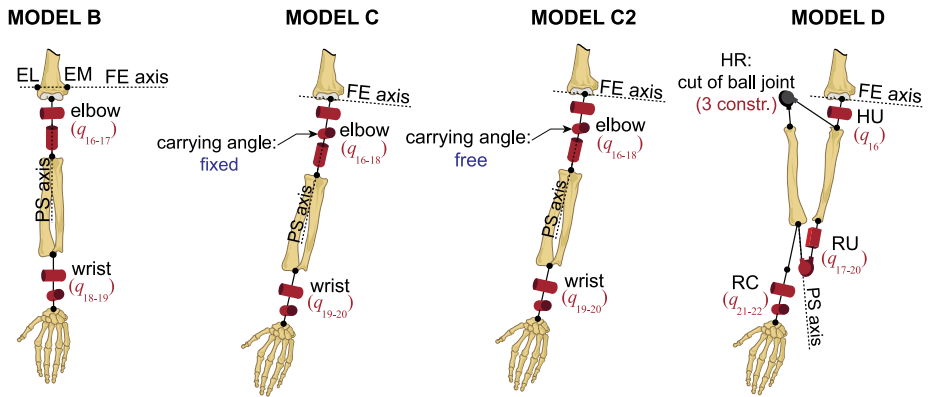
Fig. 3 Schematic of the four comparative forearm models (B, C, C2 and D) according to different assumptions. The DoFs q_{1-15} are the same as model A. See Tables 5, 6, 7, 8 of Appendix A for a detailed description of the kinematic chains

the elbow joint rotations [5, 6]. This elbow functional LCS uses the personalized FE axis computed through the SARA method [39, 40] as the mediolateral axis (see Appendix B, adapted from [6]). The use of functional LCS reduces the kinematic cross-talk [6, 8].

3.1.4 Reference configuration

The reference pose configuration is defined such that the forearm kinematics is easily interpretable and the error is evenly spread over the full range of amplitude, as recommended by Kontaxis et al. [6]. Therefore, a correction of the forearm and hand poses is applied in such a way that the reference configuration is midway between full flexion and extension as well as midway between full forearm pronation and supination (neutral position).

3.2 Comparative models

The proposed model (model A) is compared to four conventional models (models B, C, C2 and D) that consider specific modeling assumptions of the literature concerning the forearm kinematic model (Fig. 3).

Since the current study focuses on the impact of a refined forearm model, q_{1-15} are the same for the five models. Models B, C, and C2 present the forearm as one rigid body, connected by two anatomical joints, namely the elbow and the wrist. Model B represents the most typical and widely used model [6], recognized by the ISB [35]. This model represents the elbow FE and PS DoFs with two orthogonal revolute joints, q_{16} and q_{17}, respectively. Note that no personalization of the joint parameters is performed for this model. Models C and C2 introduce the carrying angle (q_{17}) between the FE (q_{16}) and PS (q_{18}) DoFs, but according to a different assumption: fixed (model C, e.g., [8]) or free (model C2, e.g., [4, 27, 29]). The carrying angle value of model C is fixed by an experimental measurement using a goniometer, as reported in Sect. 3.3. Model D presents a closed-loop system articulating the ulna and the radius through the HU (q_{16}), RU (q_{17-20}), and HR (cut of ball joint with three kinematic loop-closure constraints) joints. This kinematic chain is similar to the one presented by Pennestrì et al. [3]. Finally, CoRs and AoR of models C, C2, and D are personalized in the same way as model A where applicable.

Note that even if the total number of generalized coordinates is different between the closed and open-loop models, the five models have a comparable number of DoFs (model A, $23 - 3$ loop-closure constraints $= 20$ DoFs; model B, 19 DoFs; model C, 20 DoFs; model C2, $20 - 1$ fixed angle $= 19$ DoFs; model D, $22 - 3$ loop-closure constraints $= 19$ DoFs).

3.3 Kinematic data acquisition

The experiments were performed by 15 adults, healthy, and free from upper limb pathology (Table 1).

The study was approved by the institutional ethical committee and all participants gave their informed consent. As shown in Figs. 4–5 and described in Appendix C, 29 reflective markers (9 mm diameter) were placed on the dominant upper extremity of each subject, ensuring a minimum of four markers per rigid body for redundancy: thorax (4), clavicle (4), scapula (4), humerus (5), ulna (4), radius (4), and hand (4). This marker set includes anatomical markers (represented in black) located on bony landmarks as prescribed by the ISB [35], and is complemented by technical markers (represented in white), which are chosen to minimize soft tissue artefacts [42]. The 3D marker trajectories were collected at 100 Hz by a motion capture system composed of 12 cameras (T40S, Vicon-Oxford, UK).

The kinematic data acquisition has two main sources of error: the experimental error of the motion capture system and the soft tissue artefacts. In the first case, the accuracy of the data acquisition depends on the quality of the system and equipment used as well as some parameters related to experimental setup such as the number of cameras and their placement, the volume of study, the number and the size markers. With commercial systems of last generation such as the one used in this context study, an accuracy of about 1 mm is expected [43]. To reduce the high frequency measurement noise, marker trajectories were processed using a singular spectrum analysis [44]. Rather than being based on an arbitrary cut-off frequency like in conventional low-pass filters (e.g., Butterworth filter), this method decomposes the original signal into a few additive and independent components that are used to reconstruct the signal. Therefore, this approach facilitates the extraction of the signal latent trend from the inherent random noise contained in the experimental acquisition [44]. The second source of error arises from the use of skin markers to capture the kinematics of the movement. The motion of soft tissue can be relative to the underlying bone or between markers [42, 43, 45, 46].

Prior to the dynamic tasks of interest, a static position was recorded to personalize the geometric parameters, i.e., the segment lengths, the technical LCS and the marker relative coordinates. Each subject then performed successive 3D functional movements involving each DoF at every anatomical joint such as flexion–extension, abduction–adduction, and circumduction movements [47]. These movements serve to determine functional and personalized joint parameters using the SCoRE [38] and SARA [39, 40] methods, respectively. Afterwards, since there are no standardized dynamic activities for the upper extremity analysis

Table 1 Subject characteristics

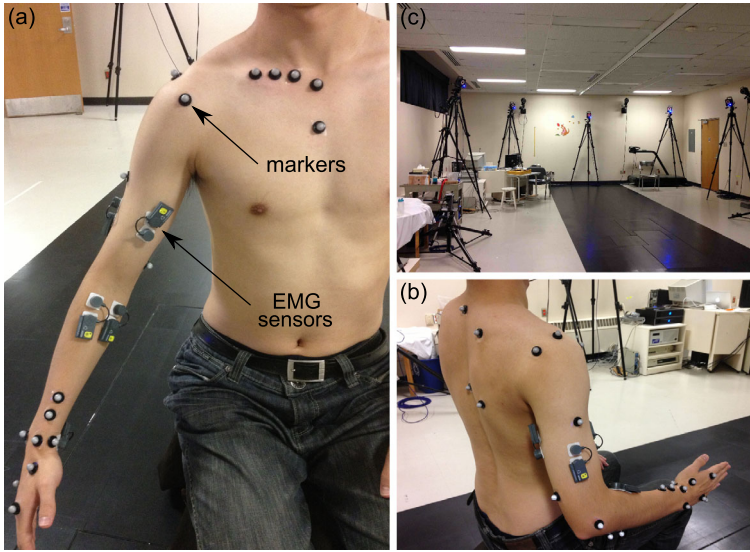|	Female ($N = 5$)	Male ($N = 10$)
Age (y)	24 ± 2	27 ± 6
Height (m)	1.68 ± 0.07	1.78 ± 0.06
Weight (kg)	57.3 ± 2.9	76.2 ± 8.5
Carrying angle (°)	10 ± 3	8 ± 2

Fig. 4 (**a**) Anterior and (**b**) posterior views of a subject equipped with reflective markers and electromyography (EMG) sensors for the purpose of future studies. (**c**) Motion capture system composed of 12 cameras
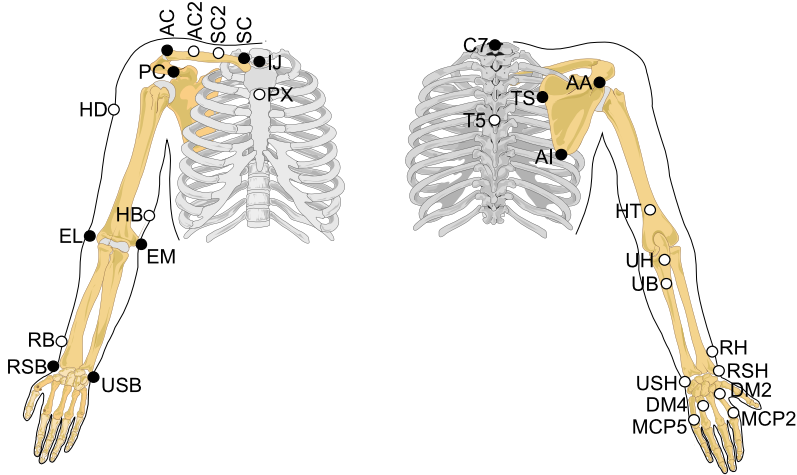

Fig. 5 Marker placement including anatomical (*in black*) and technical (*in white*) markers. See Appendix C for a detailed description of the marker locations

[4, 6] like gait at the lower limb, pure flexion–extension (FE) and pronation–supination (PS) tasks were selected as the studied dynamic tasks to facilitate data analysis. Each task was cyclically performed for five cycles at a controlled cadence of 0.5 Hz using a metronome.

3.4 Inverse kinematics: a global optimization including loop closure

The inverse kinematics problem is formulated as a global optimization (GO) problem. The optimal pose of the multibody model is computed for each data frame such that the differ-

ence between the experimental and model-determined marker coordinates is globally mini-
mized in a least squares sense [22, 48, 49]. This approach has been termed the global method
by Lu and O'Connor [48] since the minimization is performed in terms of a global criterion
including all markers and segments, in contrast to local approaches where segments are pro-
cessed independently [50, 51]. For the closed-loop multibody systems (models A and D),
the optimization is formulated as a constrained nonlinear problem. Mathematically, the min-
imization problem can be defined by the objective function formulated as follows:

$$\min_{q} f(q) = \sum_{m=1}^{n_m} \left\| X_{\mathrm{mod},m}(q) - x_{\mathrm{exp},m} \right\|^2 \tag{1}$$

$$\text{subject to:} \quad h_{\mathrm{loop}}(q) = 0$$

where q is the vector of joint generalized coordinates of the multibody model and is
the design variable of the optimization process; m indicates the marker index ($n_m = 29$);
$X_{\mathrm{mod},m}(q)$ are the marker coordinates obtained using the forward kinematic function of
the multibody system; $X_{\mathrm{exp},m}$ are the experimental marker coordinates provided by the
kinematic data acquisition; and finally, $h_{\mathrm{loop}}(q)$ represents the kinematic loop-closure con-
straints, where applicable, that must be fulfilled. Note that the objective function $f(q)$ is
solved independently at each time frame as a static optimization, and thus is not time-
dependent in its definition.

The GO is implemented according to a threefold purpose. First, this global approach
based on the a priori definition of a kinematic chain avoids dislocation and allows the dele-
terious effects of the noise generated by the use of skin markers to be reduced. Secondly,
this optimization process verifies the kinematic constraint equations at each time step by
calling the forward kinematic function, and therefore ensures kinematic data consistency at
position level. Finally, this GO directly provides the joint generalized coordinates required
to drive the multibody model in the inverse dynamic analysis.

3.5 Inverse dynamics

3.5.1 Personalized body segment inertial parameters

The body segment inertial parameters (BSIP) may influence the results of the inverse dy-
namic analysis [52]. Therefore, in this study the BSIP of the arm, forearm, and hand are
personalized using the geometric model of Yeadon [53], requiring 18 anthropometric mea-
surements of the upper limb. Since Yeadon's model does not distinguish the radius and the
ulna, the BSIP of the forearm are equally distributed between the two bones. Unlike the so-
called proportional methods based on predictive regression equations such as Winter [54],
Zatsiorsky [55], and de Leva [56], this geometric method allows different types of mor-
phologies to be distinguished as well as the impaired and normal limbs of a subject to be
compared. This distinction is essential for applications with atypical populations. The BSIP
of the thorax, clavicle, and scapula are estimated from literature based on MRI [57] or set to
negligible values when not available in the literature.

3.5.2 Equations of motion

The multibody dynamic equations are symbolically generated by the ROBOTRAN soft-
ware [58] based on a recursive Newton–Euler formalism, which is more efficient than other
formalisms when the number of degrees of freedom increases [59]. For the open-loop and

closed-loop models, the inverse dynamic equations of motion are given by Eqs. (2) and (3) through (6), respectively:

$$M(q)\ddot{q} + C(q, \dot{q}, g) = Q \tag{2}$$

$$M(q)\ddot{q} + C(q, \dot{q}, g) = Q + J^{\mathrm{T}}\lambda \tag{3}$$

$$h_{\mathrm{loop}}(q) = 0 \tag{4}$$

$$\dot{h}_{\mathrm{loop}}(q, \dot{q}) = J(q)\dot{q} = 0 \tag{5}$$

$$\ddot{h}_{\mathrm{loop}}(q, \dot{q}, \ddot{q}) = J(q)\ddot{q} + \dot{J}(q, \dot{q})\dot{q} = 0 \tag{6}$$

where $M(q)$ is the system generalized mass matrix; C is the nonlinear dynamic vector that contains the gyroscopic, centrifugal effects, and the contribution of gravity g; Q is the generalized force vector; J is the symbolic Jacobian matrix of the kinematic loop-closure constraints provided by the ROBOTRAN software, $J = \frac{\partial h_{\mathrm{loop}}}{\partial q^{\mathrm{T}}}$; and finally, λ is the vector of Lagrange multipliers related to the kinematic loop-closure constraints.

The joint generalized coordinates q are approximated by cubic smoothing splines to ensure continuity, and the corresponding velocities $\dot{q}$ and accelerations $\ddot{q}$ are analytically calculated using spline differentiation techniques. Afterwards, using the BSIP and the generalized positions, velocities, and accelerations $(q, \dot{q}, \ddot{q})$, the problem can be solved at each time frame using an inverse dynamic analysis. Note that for the models subject to kinematic loop-closure constraints, the equations of motion are reduced in the ROBOTRAN software using both the coordinate partitioning method [58] and a decomposition of the generalized force vector Q into active and passive components where there are as many active components as DoFs [60]. In this study, the ROBOTRAN software has been chosen for two main reasons: its computation time efficiency in the various processes, enabled by an automatic 30 % reduction in the number of operations [61], and an ease of handling in multiphysics modeling [62]. The ROBOTRAN software, combined with MATLAB®, Simulink® or C, enables a flexibility of choice between integrators and time step sizes [58], and also provides modal analyses, equilibrium analyses, and dynamic parameterization [59]. These features would be useful for further applications in forward dynamics and optimal control simulation.

3.6 Model comparison

The proposed model A is compared to the four conventional models (B, C, C2, and D) in terms of (i) the global and local movement reconstruction errors during inverse kinematics and (ii) the joint torque-angle patterns. To measure the performance of each model to fit the experimental kinematic data during both dynamic tasks, the global movement reconstruction error (E) of the inverse kinematics optimization is defined as the root mean square error between the 3D coordinates predicted by the model and the 3D marker coordinates experimentally acquired by the cameras as follows:

$$E = \frac{1}{n_f} \sum_{f=1}^{n_f} \sqrt{\sum_{m=1}^{n_m} \left\| X_{\mathrm{mod},(m;f)}(q) - X_{\mathrm{exp},(m;f)} \right\|^2} \tag{7}$$

where f indicates the frame index and n_f is the total number of frames. The decomposition of the global error $(m = [1, \ldots, 29])$ into local errors at the arm $(m = [13, \ldots, 17])$, forearm $(m = [18, \ldots, 25])$, and hand $(m = [26, \ldots, 29])$ is also analyzed.

Fig. 6 Global reconstruction
error of the five models (A, B, C,
C2, and D) during the two
dynamic tasks
(FE, flexion–extension;
PS, pronation–supination).
The values are given as mean and
standard deviation for the
15 subjects
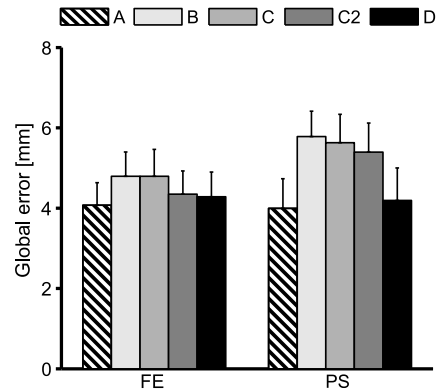
As complementary information, the computational time per frame of the movement reconstruction process during the GO is expressed as the CPU time per frame (PC, Intel® Xeon® CPU E5607, 2.27 GHz). Joint kinematics and dynamics of each model are expressed through the joint torque-angle pattern and compared for each corresponding DoF to assess minimum, maximum, and range differences. Joint torques (T) are normalized to dimensionless values (T_0) with respect to half of the body weight times the length of the upper limb for each subject [13, 63] as follows:

$$T_0 = \frac{T}{0.5mgl} \tag{8}$$

where m is the total mass of the subject; g is the gravitational constant; and l is the total length of the upper limb. The results are then time-normalized to a typical cycle and averaged through the 15 subjects for each task.
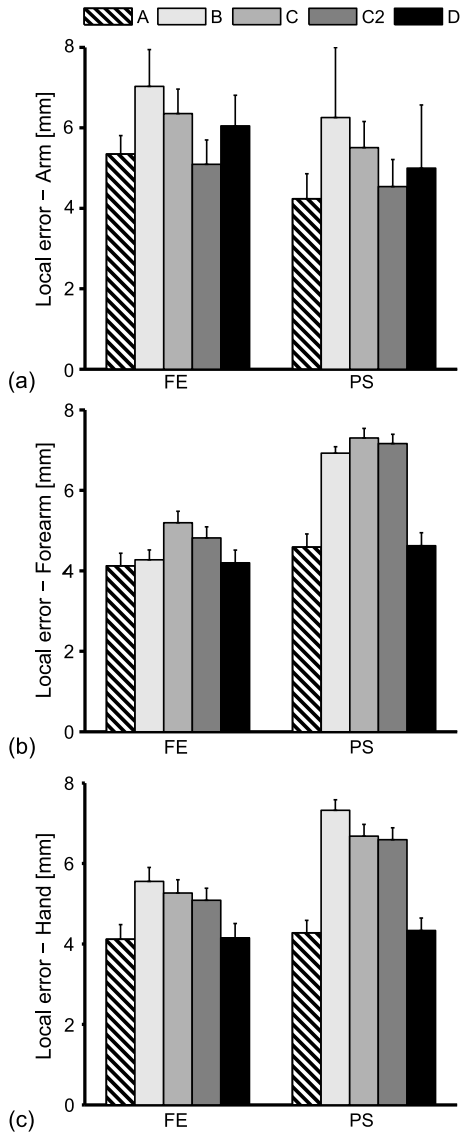
4 Results

This section presents the comparative results between the five models concerning the movement reconstruction errors and the joint kinematics and dynamics.

4.1 Movement reconstruction errors

The comparison of the global reconstruction error between the five models shows that the proposed model (A) leads to the lowest error for each task, 4.1 ± 0.6 mm for the FE task and 4.0 ± 0.7 mm for the PS task (Fig. 6). For the FE task, the global reconstruction error of model A represents a decrease of 15 %, 15 %, 6 %, and 5 % in comparison to models B, C, C2, and D, respectively. This decrease is even larger for the PS task: 31 %, 29 %, 26 %, and 5 % in comparison to models B, C, C2, and D, respectively. The two closed-loop models (A and D) present a better global reconstruction of the movement, in comparison to the three open-loop models (B, C, and C2). Among the latter, model C2 performs better than models B and C during both tasks. No noticeable difference is observed between models B and C during the FE task, but the global reconstruction error is lower for model C (5.8 ± 0.6 mm) over model B (5.6 ± 0.7 mm) during the PS task.

Fig. 7 Local reconstruction errors of the five models (A, B, C, C2, and D) at the (**a**) arm, (**b**) forearm, and (**c**) hand during the two dynamic tasks (FE, flexion–extension; PS, pronation–supination). The values are given as mean and standard deviation for the 15 subjects

The comparison of the local reconstruction errors between the five models at the arm (Fig. 7(a)), forearm (Fig. 7(b)) and hand (Fig. 7(c)) shows slightly different tendencies from the global reconstruction error. The results with models A and D remain similar except for the arm local reconstruction error where model D presents an increase of 12 % and 15 % for the FE and PS tasks, respectively. However, models A and D largely reduce the local reconstruction error at the forearm and hand during the PS task. When compared to models B, C, and C2, the local error reduction provided by model A is approximately 34 %, 37 %, 36 % for the forearm and 42 %, 36 %, 35 % for the hand. Among the three open-loop models, model C2 presents better local reconstruction errors than the two other models at the arm and hand while model B provides the lowest local error at the forearm. Finally,

model A provides the lowest local errors, except at the arm during the FE task where it is 0.2 mm higher than model C2.

During the FE task, the mean computational times per frame during the GO for models A, B, C, C2, and D are 99 ± 41 ms/fr, 85 ± 27 ms/fr, 107 ± 40 ms/fr, 84 ± 37 ms/fr, and 95 ± 42 ms/fr, respectively. During the PS task, these mean computational times per frame for models A, B, C, C2, and D are 94 ± 33 ms/fr, 87 ± 35 ms/fr, 97 ± 28 ms/fr, 95 ± 53 ms/fr, and 90 ± 32 ms/fr, respectively. The largest difference is found between models C and C2 during the FE task (23 ms/fr), and between models C and B during the PS task (10 ms/fr). No notable tendency is observed between models. The mean computational times for the two tasks are similar: an average of 94 ms/fr for the FE task and an average of 93 ms/fr for the PS task. Therefore, no notable difference is obtained between tasks.

4.2 Joint kinematics and dynamics

During the FE task, the joint kinematics and dynamics of the five models, expressed as the torque-angle pattern of the main DoF, differ without any particular tendency (Fig. 8(a)). However, differences are observed for the PS task, where the forearm model refinement clearly affects the five patterns (Fig. 8(b)).

Minimum, maximum, and range of elbow FE and PS angles and torques during each mean cycle of the two dynamic tasks are reported in Tables 2 and 3, respectively.

Concerning the FE task, the results yielded by the five models are similar. The average FE ranges are approximately 131°. The largest difference on the normalized FE joint torques is found between models A and C, with $11.3 \times 10^{-3} \pm 2.9 \times 10^{-3}$ versus $10.2 \times 10^{-3} \pm 2.9 \times 10^{-3}$, i.e., 11 %.

Concerning the PS task, the results show that the joint-angle pattern is affected by the model. The PS angle ranges are $140 \pm 22°$ and $141 \pm 21°$ for models A and D respectively while for models B, C, and C2 these ranges are $111 \pm 18°$, $115 \pm 20°$, and $114 \pm 20°$, respectively. Therefore, the closed-loop models (A and D) increase the PS ranges by approximately 24 % in comparison to the open-loop models (B, C and C2). Minimum and maximum values of the normalized PS joint torques are also different from one model to another. In particular, the torque-angle pattern of model B is underestimated when compared to other patterns. Nevertheless, the normalized PS joint torque ranges for models B, C, C2, and D are around the same average value of 2.5×10^{-3}. Model A results in the highest maximum and range during the PS task, namely approximately 24 % higher than other models. Therefore, even if models A and D present similar PS angle ranges, normalized PS joint torque ranges are underestimated in model D, as well as in other comparative models.

5 Discussion

The general objective of this paper was to refine the upper limb joint kinematics and dynamics using a subject-specific closed-loop forearm model. This was achieved by including into the kinematic chain the two forearm bones as separate bodies articulated by the HU, HR and RU joints, as well as personalized joint parameters. To assess this refinement, four multibody models were built according to conventional literature assumptions and were compared to the proposed model in terms of the movement reconstruction errors and the joint kinematics and dynamics. The studied tasks, namely FE and PS, were performed by 15 adults to evaluate the method and the proposed model on a significant population.

Fig. 8 Normalized torque-angle pattern of the five models (A, B, C, C2, and D) during the (**a**) flexion–extension (FE) and (**b**) pronation–supination (PS) tasks. The values are given as mean for the 15 subjects (Color figure online)
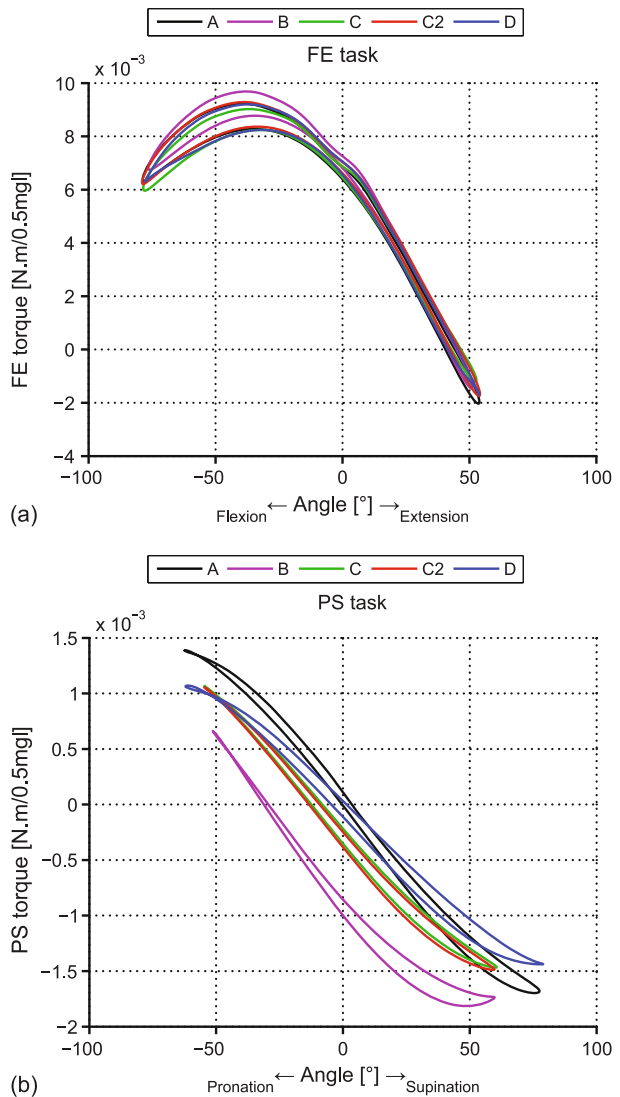
5.1 Results analysis

5.1.1 Impact on movement reconstruction errors

The reported movement reconstruction errors confirm the considerable interest of taking into account the interactions between the ulna and radius rather than considering the forearm as one single rigid body. The reduced local reconstruction errors of the proposed model (A) during the PS task suggest that this model not only improves the pose of the forearm, but also the pose of the arm and hand, when compared to the three conventional models representing the forearm as an open-loop system. This is of particular importance since the hand position often determines the achievement of a functional task [4]. Similar results are obtained for the other closed-loop model (D) in this study, except for the arm segment where

Table 2 Minimum (min), maximum (max), and range of elbow FE and PS angles during flexion–extension (FE) and pronation–supination (PS) tasks, respectively. The values are given as mean and standard deviation for the 15 subjects

Model	FE angle during FE task [°]			PS angle during PS task [°]		
	min	max	range	min	max	range
A	-78.6 ± 9.1	53.9 ± 9.1	132.6 ± 18.2	-62.4 ± 11.1	77.5 ± 11.1	139.9 ± 22.2
B	-76.5 ± 9.0	51.2 ± 9.0	127.7 ± 18.0	-51.3 ± 9.0	59.8 ± 9.0	111.1 ± 17.9
C	-78.5 ± 9.3	52.8 ± 9.3	131.2 ± 18.7	-54.7 ± 10.1	60.6 ± 10.1	115.3 ± 20.3
C2	-78.9 ± 9.4	54.2 ± 9.4	133.1 ± 18.9	-54.7 ± 9.8	59.6 ± 9.8	114.3 ± 19.7
D	-77.8 ± 9.1	53.9 ± 9.1	131.6 ± 18.2	-62.1 ± 10.4	79.0 ± 10.4	141.0 ± 20.8

Table 3 Minimum (min), maximum (max), and range of elbow FE and PS normalized torques during flexion–extension (FE) and pronation–supination (PS) tasks, respectively. The values are given as mean and standard deviation for the 15 subjects

Model	FE normalized torque during FE task [N.m/0.5 mgl $\times 10^{-3} \times 10^{-3}$]			PS normalized torque during PS task [N.m/0.5 mgl $\times 10^{-3}$]		
	min	max	range	min	max	range
A	-2.0 ± 1.5	9.2 ± 1.5	11.3 ± 2.9	-1.7 ± 0.5	1.4 ± 0.5	3.1 ± 1.0
B	-1.5 ± 1.5	9.7 ± 1.5	11.2 ± 3.0	-1.8 ± 0.6	0.7 ± 0.6	2.5 ± 1.1
C	-1.2 ± 1.5	9.0 ± 1.5	10.2 ± 2.9	-1.5 ± 0.5	1.1 ± 0.5	2.5 ± 1.1
C2	-1.7 ± 1.5	9.3 ± 1.5	11.0 ± 3.0	-1.5 ± 0.5	1.1 ± 0.5	2.5 ± 1.0
D	-1.7 ± 1.5	9.2 ± 1.5	10.9 ± 2.9	-1.4 ± 0.5	1.1 ± 0.5	2.5 ± 1.0

the local reconstruction error was higher. Model B is not realistic since it oversimplifies the relative pose of the elbow FE and PS AoRs. The integration of a free carrying angle between the FE and PS angles (model C2) leads to a better reconstruction of the FE and PS tasks when compared to a fixed carrying angle (model C). Concerning the FE movement, a few studies have mentioned the important role of the carrying angle and its linear relation with the FE angle [26–28]. Therefore, this finding is also in line with the fact that the carrying angle varies during FE, thus explaining the better results obtained by model C2 during the FE task. According to the results of the proposed model, one can conclude that the use of a specific kinematic chain that better mimics the anatomical joints of the forearm provides fewer movement reconstruction errors as well as less compensation at the surrounding segments.

If we examine the dispersion of the global reconstruction error around the average (Fig. 6), it is possible to see a relatively low value of the standard deviations, equal to about 0.6 mm and 0.7 mm during the FE and PS, respectively, for the five models. This indicates a similar and low inter-subject variability regardless of the model used. These deviations are even lower in local reconstruction errors at the forearm and hand. This shows that the reduction of the error, and therefore the better representation of movement forearm and hand, is due to the model and not the effect between subjects. Regarding the intra-subject variability in the comparison of models, it was rejected because the five models have exactly the same kinematic inputs. Each subject is her/his own control in such repeated measures statistics. It is therefore possible to isolate the effect of the model for each subject. Further statistical analysis should be conducted to confirm a statistically significant effect of the model.

Within this study, several recognized techniques were applied to minimize soft tissue artefacts during the experimental protocol and the calculation process. To minimize the

variation of distance between markers during the reconstruction of motion and calculation of segmental lengths, distances between markers were averaged based on a static position where there is practically no skin movement. This static position was the subject position when installing skin markers to introduce less error. Furthermore, the anatomical marker set was complemented with technical markers to ensure an information redundancy.

5.1.2 Impact on joint kinematics and dynamics

This study highlights the fact that the level of refinement of the forearm multibody model can strongly affect the joint kinematics and dynamics during the PS task. Indeed, the range of motion of the proposed model is about 140° during the PS task while it is approximately 114° for the other conventional models. The ranges of motion obtained by the closed-loop models (A and D) are more in agreement with the normally known values for physiological conditions in healthy subjects [24, 34]. The PS ranges reported in this study for open-loop models are closed to those ones reported by Cutti et al. [5] and Fohanno et al. [8], namely around 114°.

Unlike during the FE task, the assumption made on the carrying angle in conjunction with personalized joint parameters affects the joint dynamics during the PS task. The model proposed by the ISB (model B) shows a different joint-angle pattern, which underestimates the angle and torque ranges when compared to the proposed model. In regard to models C and C2, the results show that defining a subject-specific and a fixed carrying angle in the kinematic model has little effect on the principal angles and torques in comparison to those ones obtained with no specified carrying angle. However, the torque-angle patterns of the three open-loop models are underestimated when compared to the proposed model. Finally, although the joint angles of the closed-loop models (A and D) present similar ranges, the reported joint torque ranges are underestimated by approximately 24 % in model D. Since inverse dynamics is a deterministic process, i.e., providing a single solution of the joint generalized force vector for a given kinematic configuration of a model, the closed-loop models, which best fit the experimental kinematic data, also provide more realistic joint torques. This is of greatest importance in biomedical applications requiring a biofidelic quantification of joint torques.

5.2 Global optimization with loop closure

This study presents the first closed-loop model of the upper limb that uses a GO approach [48] to reconstruct joint kinematics as well as an inverse dynamic analysis to determine internal efforts during movement. Other similar studies have modeled the forearm as an open-loop system [22, 64]. The GO problem is addressed using a constrained nonlinear least squares minimization where the fulfillment of the equations of motion and kinematic closure are enforced. The optimization fits the experimental data with acceptable global movement reconstruction errors ranging from 4 to 6 mm. The movement reconstruction errors are in close agreement with studies using a similar approach at the upper limb [8, 65]. Furthermore, the comparison of the computational time per frame between the five models to reconstruct the FE and PS tasks shows that even if the level of refinement is increased, the computational time of the proposed model is similar to the other models. Kinematic loop-closure constraints usually increase the difficulty of movement reconstruction by offering fewer possible solutions for the model configuration. An appropriate closed-loop kinematic chain is therefore imperative to provide a biofidelic representation of the forearm osteoarticular system, and that with comparable computational time.

Another challenge that needs to be highlighted in the inverse kinematics of the forearm is the relative rotation between the skin markers attached to the proximal and distal ends of the forearm during PS. The PS movement is not a simple hinge-like motion, but a complex motion with rotational and translational components gathered in a closed-loop between the humerus, ulna and radius. However, when the forearm is considered as one single rigid body, the skin markers of the forearm are not allowed to have a relative motion, and therefore cannot reproduce a realistic path motion. This aspect can explain the better ability of the closed-loop models to fit the trajectories of the experimental data, and that with comparable computational time during the GO process. Indeed, the closed-loop kinematic chain proposed in this study allows the distinction between the proximal markers related to the ulna and the distal markers related to both the ulna and radius. The proximal markers principally serve to identify the FE DoF, and the distal markers principally serve to identify the DoFs associated with PS. This novel approach is essential to obtain a realistic movement reconstruction of the forearm marker trajectories. To the authors' knowledge, no study has addressed this issue before. A distinction should be made between the proximal and distal markers of the forearm when reconstructing the forearm PS movement since they do not undergo the same rotational path.

5.3 Forearm axis defined by a closed-loop mechanism

There is still disagreement concerning the definition of the forearm PS AoR. It is often defined as the line connecting the HR and wrist CoRs [66], but a few authors have also used the carrying angle to define the orientation of the PS axis relatively to the FE axis [8]. However, in this study the introduction of a fixed and experimentally estimated carrying angle (model C) to identify the orientation of the PS axis does not provide better results than the model C2, which allows the carrying angle to vary over time. Besides, Fohanno et al. [8] used functional methods to determine the PS axis and it was integrated by a fixed carrying angle value. Nevertheless, the main drawback of using such functional methods for internal–external rotational movement like PS is that it is generally less accurate than with flexion–extension and abduction–adduction movements due to the larger relative movement between markers and the underlying bone [67]. This issue is overcome in the proposed model by introducing the surrogate mechanism of Kecskeméthy and Weinberg [2], which already takes into account the movement of the forearm axis during motion. The forearm axis is therefore expressed between the HR and RU joints as a result of the DoFs found in the parallel closed-loop mechanism. By means of a swaying angle and a lateral displacement of the ulna with respect to the humerus, the present model also integrates the concept of carrying angle. The proposed model has a better ability to reproduce the FE task with a reduction of the movement reconstruction errors.

5.4 Personalized joint parameters

Another novel aspect that is demonstrated in this study is the feasibility of personalizing the lengths and the CoRs comprising the theoretical forearm mechanism presented by Kecskeméthy and Weinberg [2]. This leads to a non-ideal and subject-specific mechanism instead of a mechanism that lies parallel and planar in full supination. Indeed, this study provides a functional definition of the HU, HR, and RU joints comprising the theoretical closed-loop mechanism by means of the SCoRE [38] and SARA [39, 40] methods. As demonstrated by a few authors [5, 8, 37], the use of functional LCS minimizes kinematic cross-talk. Further studies are required to study the interactions between the forearm DoFs and properly assess the elbow kinematic cross-talk. Forearm closed-loop models may be less prone to the kinematic coupling problem between the FE and PS DoFs at the elbow.

5.5 Limitations and perspectives of the study

Within this study, simple tasks are considered to facilitate the interpretation of the results. While some insight has been gained into the coupling of forearm FE and PS DoFs, additional work is required to attest the proposed model for more complex dynamic tasks and to obtain normative values concerning functional tasks. Although only a small benefit of the proposed model is observed during the pure FE task when compared to the largely improved results obtained during the pure PS task, the proposed model may significantly minimize kinematic cross-talk during functional tasks requiring combined elbow FE and PS. Furthermore, the introduction of a more complex shoulder mechanism may improve the kinematic cross-talk during functional tasks. Similarly, it is foreseen that a detailed model of the wrist and the hand may improve the quantification of the upper limb kinematics and dynamics in dexterity tasks.

Recently, it was evoked that the ulna and the radius both perform an arc of circumduction at the distal end of the forearm during the PS motion [24] (see Fig. 9(a) of Appendix D). As mentioned by the author, this circumduction motion is a combination of abduction–adduction and flexion–extension movements of the ulna in the sagittal plane. This latter flexion–extension DoF is not included in the kinetostatic mechanism proposed by Kecskeméthy and Weinberg [2], where the ulna is allowed to have an axial displacement and a lateral swaying with respect to the humerus only. It is therefore theoretically restricted to a planar abduction–adduction motion at the distal end (see Fig. 9(b) of Appendix D). Future work in imaging concerning the coupling between the elbow and the distal RU joints may improve the reconstruction of the PS motion and its distal circular path as described in [24].

6 Conclusion

To conclude, this study shows that existing forearm models are mainly lacking in a biofidelic representation of the interaction between the forearm bones resulting in limited capabilities. This study provides a comprehensive description of a biofidelic osteoarticular multibody model of the forearm and its benefits on joint kinematics and dynamics of the upper limb. This model is intended to take into account the complex movement of the forearm, including FE and PS movements, but also more complex tasks combining both movements. In this work, a novel methodology is adopted and properly incorporated to achieve an integrated and refined forearm model that improves joint pose definition during FE and PS tasks. This refinement is achieved without increasing the computational effort of the optimization process when compared to the simpler models. Particular attention has been paid to minimize soft tissue artefacts during the experimental protocol and the calculation process, as well as to provide personalized BSIP. The current study demonstrates that subject-specific and closed-loop modeling of the forearm is a key-step to the realistic representation of the forearm PS motion. A similar approach can be extended to other anatomical joints or limbs. A proper estimation of joint kinematics is essential to accurate internal efforts quantification and may provide clinically meaningful information. A biofidelic representation of the two forearm bones may also provide better muscle insertion sites in upper limb musculoskeletal modeling, which is a topic of great interest in biomechanics. Future work could also analyze this refined model in forward dynamics and optimal control simulation frameworks.

Appendix A: Kinematic chains of the models

Table 4 Kinematic chain description of the proposed model (A)

Joint	Proximal segment	Distal segment	DoFs	q_i	Local axis	Functional description
Moving base	Base	Thorax	6	q_1	Z	Medial/lateral translation
				q_2	Y	Vertical translation
				q_3	X	Anterior/posterior translation
				q_4	Z	Flexion/extension
				q_5	X	Lateral rotation
				q_6	Y	Axial rotation
Sternoclavicular (SC)	Thorax	Clavicle	3	q_7	Y	Protraction–retraction
				q_8	X	Depression/elevation
				q_9	Z	Axial rotation
Acromioclavicular (AC)	Clavicle	Scapula	3	q_{10}	Y	Protraction/retraction
				q_{11}	X	Lateral/medial rotation
				q_{12}	Z	Anterior/posterior tilt
Glenohumeral (GH)	Scapula	Humerus	3	q_{13}	Y	Plane of elevation
				q_{14}	X	Negative elevation
				q_{15}	Y	Axial rotation
Humeroradial (HU)	Humerus	Ulna	1	q_{16}	Z	Flexion/extension
			Closed-loop: $5 - 3 = 2$ DoFs	q_{17}	X	Axial displacement
				q_{18}	Y	Lateral swaying
Radioulnar (RU)	Ulna	Radius		q_{19}	X	Pronation/supination
				q_{20}	Y	Torsional angle
Virtual CoR	Ulna	Radius		q_{21}	Z	Aperture angle
Humeroradial (HR)	Radius	Humerus		–		Cut of ball joint with 3 constraints
Radiocarpal (RC)	Radius	Hand	2	q_{22}	Y	Flexion/extension
				q_{23}	Z	Ulnar/radial deviation

Table 5 Kinematic chain description of model B

Joint	Proximal segment	Distal segment	DoFs	q_i	Local axis	Functional description
q_{1-15} are the same as model A (see Table 4)						
Elbow	Humerus	Forearm	2	q_{16}	Z	Flexion/extension
				q_{17}	Y	Pronation/supination
Wrist	Forearm	Hand	2	q_{18}	Y	Flexion/extension
				q_{19}	Z	Ulnar/radial deviation

Table 6 Kinematic chain description of model C

Joint	Proximal segment	Distal segment	DoFs	q_i	Local axis	Functional description
q_{1-15} are the same as model A (see Table 4)						
Elbow	Humerus	Forearm	3	q_{16}	Z	Flexion/extension
				q_{17}	Y	Carrying angle (fixed)
				q_{18}	X	Pronation/supination
Wrist	Forearm	Hand	1	q_{19}	Y	Flexion/extension
				q_{20}	Z	Ulnar/radial deviation

Table 7 Kinematic chain description of model C2

Joint	Proximal segment	Distal segment	DoFs	q_i	Local axis	Functional description
q_{1-15} are the same as model A (see Table 4)						
Elbow	Humerus	Forearm	3	q_{16}	Z	Flexion/extension
				q_{17}	Y	Carrying angle (free)
				q_{18}	X	Pronation/supination
Wrist	Forearm	Hand	2	q_{19}	Y	Flexion/extension
				q_{20}	Z	Ulnar/radial deviation

Table 8 Kinematic chain description of model D

Joint	Proximal segment	Distal segment	DoFs	q_i	Local axis	Functional description
q_{1-15} are the same as model A (see Table 4)						
Humeroradial (HU)	Humerus	Ulna	1	q_{16}	Z	Flexion/extension
Radioulnar (RU)	Ulna	Radius	Closed-loop: $4-3=1$ DoF	q_{17}	X	Axial displacement
				q_{18}	X	Pronation/supination
				q_{19}	Y	Torsional angle
				q_{20}	Z	Aperture angle
Humeroradial (HR)	Radius	Humerus		–		Cut of ball joint with 3 constraints
Radiocarpal (RC)	Radius	Hand	2	q_{21}	Y	Flexion/extension
				q_{22}	Z	Ulnar/radial deviation

Appendix B: Functional local coordinate system

The functional LCS based at the HU joint, intended to describe the forearm rotations, is built as follows (adapted from [6]):

- $Z_{HU} = AoR_{FE}/\|AoR_{FE}\|$: pointing lateral
- $X_{HU} = Y_{H1} \times Z_{HU}/\|(Y_{H1} \times Z_{HU})\|$: pointing forward
- $Y_{HU} = Z_{H1} \times X_{HU}/\|(Z_{H1} \times X_{HU})\|$: pointing proximal

where AoR_{FE} is the flexion–extension axis of rotation of the elbow computed through the SARA method [39], while Y_{H1} is the anatomical axis of the humerus constructed as follows using the glenohumeral (GH) joint center and the mean position between the medial (EM) and lateral (EL) epicondyles ($E = (EM + EL)/2$):

- $Y_{H1} = (GH - E)/\|(GH - E)\|$: pointing proximal

Appendix C: Description of the marker locations

Table 9 Locations of the n markers on the thorax, clavicle, scapula, humerus, ulna, radius, and hand

Segment	Marker	Description
Thorax ($n = 4$)	IJ	Deepest point of incisura jugularis
	PX	Sternum, aligned with processus xiphoideus
	C7	Processus spinosus of the 7th cervical vertebra
	T5	Processus spinosus of the 5th thoracic vertebra
Clavicle ($n = 4$)	SC	Most ventral point on the sternoclavicular joint
	SC2	Lateral from sternoclavicular joint, between AC2 and SC
	AC2	Medial from acromioclavicular joint, between AC and SC2
	AC	Most dorsal point on the acromioclavicular joint
Scapula ($n = 4$)	AA	Angulus acromialis, most laterodorsal point of the scapula
	PC	Most ventral point of the processus coracoideus
	TS	Trigonum spinae scapulae, the midpoint of the triangular surface on the medial border of the scapula in line with the scapular spine
	AI	Angulus inferior, most caudal point of the scapula
Humerus ($n = 5$)	HD	Deltoid tuberosity
	HT	Posterior point near triceps muscle insertion
	HB	Medial point near biceps muscle insertion
	EL	Most caudal point on lateral epicondyle
	EM	Most caudal point on medial epicondyle
Ulna ($n = 4$)	UH	Ulna proximal point of the olecranon
	UB	Ulna distal point of the olecranon
	USH	Most caudal-medial point on the ulnar styloid, posterior
	USB	Most caudal-medial point on the ulnar styloid, anterior
Radius ($n = 4$)	RH	Distal point of the radial styloid
	RB	Proximal point of the radial styloid
	RSH	Most caudal-lateral point on the radial styloid, posterior
	RSB	Most caudal-lateral point on the radial styloid, anterior
Hand ($n = 4$)	MCP2	2nd metacarpal (distal)
	MCP5	5th metacarpal (distal)
	DM2	2nd metacarpal (proximal)
	DM4	4th metacarpal (proximal)

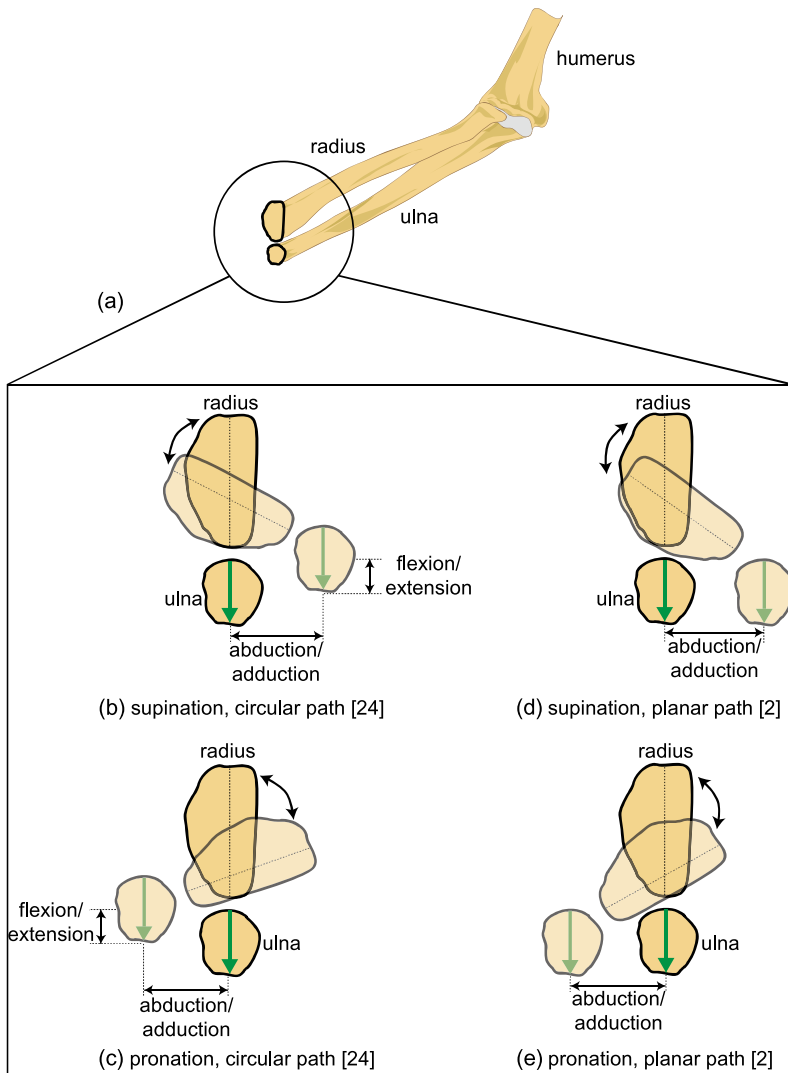## Appendix D: Theoretical paths at the distal end of the forearm

Fig. 9 Cross-sectional view of the theoretical paths of each forearm bone at the distal end. (**a**) Isometric view of the forearm. Combination of ulnar abduction–adduction and flexion–extension entailing a circular trajectory of the ulna at the distal end, as described by Amis [24] during (**b**) supination and (**c**) pronation. Ulnar flexion–extension entailing a planar trajectory of the ulna at the distal end, as described by the model of Kecskeméthy and Weinberg [2] during (**d**) supination and (**e**) pronation. The green arrow indicates that there is no axial rotation of the ulna (Color figure online)

References

1. Anglin, C., Wyss, U.P.: Review of arm motion analyses. Proc. Inst. Mech. Eng. H J. Eng. **214**(5), 541–555 (2000)
2. Kecskeméthy, A., Weinberg, A.M.: An improved elasto-kinematic model of the human forearm for biofidelic medical diagnosis. Multibody Syst. Dyn. **14**(1), 1–21 (2005)
3. Pennestrì, E., Stefanelli, R., Valentini, P.P., Vita, L.: Virtual musculo-skeletal model for the biomechanical analysis of the upper limb. J. Biomech. **40**, 1350–1361 (2007)
4. van Andel, C.J., Wolterbeek, N., Doorenbosch, C.A.M., Veeger, D.H.E.J., Harlaar, J.: Complete 3D kinematics of upper extremity functional tasks. Gait Posture **27**, 120–127 (2008)
5. Cutti, A.G., Giovanardi, A., Rocchi, L., Davalli, A., Sacchetti, R.: Ambulatory measurement of shoulder and elbow kinematics through inertial and magnetic sensors. Med. Biol. Eng. Comput. **46**(2), 169–178 (2008)
6. Kontaxis, A., Cutti, A.G., Johnson, G.R., Veeger, D.H.E.J.: A framework for the definition of standardized protocols for measuring upper-extremity kinematics. Clin. Biomech. **24**, 246–253 (2009)
7. Rettig, O., Fradet, L., Kasten, P., Raiss, P., Wolf, S.I.: A new kinematic model of the upper extremity based on functional joint parameter determination for shoulder and elbow. Gait Posture **30**, 469–476 (2009)
8. Fohanno, V., Lacouture, P., Colloud, F.: Improvement of upper extremity kinematics estimation using a subject-specific forearm model implemented in a kinematic chain. J. Biomech. **46**(6), 1053–1059 (2013)
9. Pennestrì, E., Renzi, A., Santonocito, P.: Dynamic modeling of the human arm with video-based experimental analysis. Multibody Syst. Dyn. **7**(4), 389–406 (2002)
10. Leboeuf, F., Bessonnet, G., Seguin, P., Lacouture, P.: Energetic versus sthenic optimality criteria for gymnastic movement synthesis. Multibody Syst. Dyn. **16**(3), 213–236 (2006)
11. Font-Llagunes, J.M., Barjau, A., Pàmies-Vilà, R., Kövecses, J.: Dynamic analysis of impact in swing-through crutch gait using impulsive and continuous contact models. Multibody Syst. Dyn. **28**(3), 257–282 (2012)
12. Abdullah, H.A., Tarry, C., Datta, R., Mittal, G.S., Abderrahim, M.: Dynamic biomechanical model for assessing and monitoring robot-assisted upper-limb therapy. J. Rehabil. Res. Dev. **44**, 43 (2007)
13. Desroches, G., Dumas, R., Pradon, D., Vaslin, P., Lepoutre, F.X., Chèze, L.: Upper limb joint dynamics during manual wheelchair propulsion. Clin. Biomech. **25**(4), 299–306 (2010)
14. Blana, D., Hincapie, J.G., Chadwick, E.K., Kirsch, R.F.: A musculoskeletal model of the upper extremity for use in the development of neuroprosthetic systems. J. Biomech. **41**(8), 1714–1721 (2008)
15. Jaspers, E., Desloovere, K., Bruyninckx, H., Klingels, K., Molenaers, G., Aertbeliën, E., Van Gestel, L., Feys, H.: Three-dimensional upper limb movement characteristics in children with hemiplegic cerebral palsy and typically developing children. Res. Dev. Disabil. **32**(6), 2283–2294 (2011)
16. Bolsterlee, B., Veeger, D.H.E.J., Chadwick, E.K.: Clinical applications of musculoskeletal modelling for the shoulder and upper limb. Med. Biol. Eng. Comput. **51**(9), 953–963 (2013)
17. Quental, C., Folgado, J., Ambrósio, J., Monteiro, J.: A multibody biomechanical model of the upper limb including the shoulder girdle. Multibody Syst. Dyn. **28**(1–2), 83–108 (2012)
18. Jackson, M., Michaud, B., Tétreault, P., Begon, M.: Improvements in measuring shoulder joint kinematics. J. Biomech. **45**(12), 2180–2183 (2012)
19. Senk, M., Chèze, L.: Rotation sequence as an important factor in shoulder kinematics. Clin. Biomech. **21**, S3–S8 (2006)
20. Weinberg, A.M., Pietsch, I.T., Helm, M.B., Hesselbach, J., Tscherne, H.: A new kinematic model of pro- and supination of the human forearm. J. Biomech. **33**(4), 487–491 (2000)
21. Xu, J., Kasten, P., Weinberg, A.M., Kecskeméthy, A.: Automated fitting of an elastokinematic surrogate mechanism for forearm motion from MRI measurements. In: Lenarcic, J., Stanisic, M.M. (eds.) Advances in Robot Kinematics: Motion in Man and Machine, pp. 349–358. Springer, Berlin (2010)
22. Roux, E., Bouilland, S., Godillon-Maquinghen, A.P., Bouttens, D.: Evaluation of the global optimisation method within the upper limb kinematics analysis. J. Biomech. **35**, 1279–1283 (2002)
23. Veeger, D.H.E.J., Yu, B.: Orientation of axes in the elbow and forearm for biomechanical modelling. In: Proceedings of the Fifteenth Southern Biomedical Engineering Conference, 29–31 Mar. 1996, pp. 377–380
24. Amis, A.A.: Biomechanics of the elbow. In: Stanley, D., Trail, I. (eds.) Operative Elbow Surgery. Churchill Livingstone, Elsevier, Edinburgh, New York (2012)
25. Tay, S.C., van Riet, R., Kazunari, T., Amrami, K.K., An, K.N., Berger, R.A.: In-vivo kinematic analysis of forearm rotation using helical axis analysis. Clin. Biomech. **25**(7), 655–659 (2010)
26. Goto, A., Moritomo, H., Murase, T., Oka, K., Sugamoto, K., Arimura, T., Nakajima, Y., Yamazaki, T., Sato, Y., Tamura, S., Yoshikawa, H., Ochi, T.: In vivo elbow biomechanical analysis during flexion: three-dimensional motion analysis using magnetic resonance imaging. J. Shoulder Elb. Surg. **13**(4), 441–447 (2004)

27. Zampagni, M.L., Casino, D., Martelli, S., Visani, A., Marcacci, M.: A protocol for clinical evaluation of the carrying angle of the elbow by anatomic landmarks. J. Shoulder Elb. Surg. **17**(1), 106–112 (2008)
28. Morrey, B.F., Chao, E.Y.: Passive motion of the elbow joint. J. Bone Jt. Surg. Am. **58**(4), 501–508 (1976)
29. Raison, M., Detrembleur, C., Fisette, P., Samin, J.C.: Assessment of antagonistic muscle forces during forearm flexion/extension. Multibody Dyn. Comput. Methods Appl. Sci. **23**, 215–238 (2011)
30. Gattamelata, D., Pezzuti, E., Valentini, P.P.: Accurate geometrical constraints for the computer aided modelling of the human upper limb. Comput. Aided Des. **39**, 540–547 (2007)
31. Lemay, M.A., Crago, P.E.: A dynamic model for simulating movements of the elbow, forearm, and wrist. J. Biomech. **29**(10), 1319–1330 (1996)
32. Weinberg, A.M., Pietsch, I.T., Krefft, M., Pape, H.C., van Griensven, M., Helm, M.B., Reilmann, H., Tscherne, H.: Die Pro- und Supination des Unterarms Unter besonderer Berücksichtigung der Articulatio humeroulnaris. Der Unfallchirurg **104**(5), 404–409 (2001)
33. Kasten, P., Krefft, M., Hesselbach, J., Weinberg, A.M.: Kinematics of the ulna during pronation and supination in a cadaver study: implications for ulna arthroplasty. Clin. Biomech. **19**(1), 31–35 (2004)
34. Kapandji, I.A., Honoré, L.H.: The Physiology of the Joints: The Upper Limb, vol. 1. Churchill Livingstone/Elsevier, Edinburgh, New York (2007)
35. Wu, G., van der Helm, F.C., Veeger, D.H.E.J., Makhsous, M., Van Roy, P., Anglin, C., Nagels, J., Karduna, A.R., McQuade, K., Wang, X., Werner, F.W., Buchholz, B.: ISB recommendation on definitions of joint coordinate systems of various joints for the reporting joint motion—Part II: shoulder, elbow, wrist and hand. J. Biomech. **38**(5), 981–992 (2005)
36. Piazza, S.J., Delp, S.L.: The influence of muscles on knee flexion during the swing phase of gait. J. Biomech. **29**(6), 723–733 (1996)
37. Chin, A., Lloyd, D., Alderson, J., Elliott, B., Mills, P.: A marker-based mean finite helical axis model to determine elbow rotation axes and kinematics in vivo. J. Appl. Biomech. **26**(3), 305–315 (2010)
38. Ehrig, R.M., Taylor, W.R., Duda, G.N., Heller, M.O.: A survey of formal methods for determining the centre of rotation of ball joints. J. Biomech. **39**(15), 2798–2809 (2006)
39. Ehrig, R.M., Taylor, W.R., Duda, G.N., Heller, M.O.: A survey of formal methods for determining functional joint axes. J. Biomech. **40**(10), 2150–2157 (2007)
40. O'Brien, J.F., Bodenheimer, R.E. Jr., Brostow, G.J., Hodgins, J.K.: Automatic joint parameter estimation from magnetic motion capture data. In: Proceedings of the Graphics Interface, pp. 53–60 (2000)
41. Monnet, T., Thouzé, A., Pain, M.T., Begon, M.: Assessment of reproducibility of thigh marker ranking during walking and landing tasks. Med. Eng. Phys. **34**(8), 1200–1208 (2012)
42. Cappozzo, A., Della Croce, U., Leardini, A., Chiari, L.: Human movement analysis using stereophotogrammetry: Part 1: theoretical background. Gait Posture **21**(2), 186–196 (2005)
43. Chiari, L., Croce, U.D., Leardini, A., Cappozzo, A.: Human movement analysis using stereophotogrammetry: Part 2: Instrumental errors. Gait Posture **21**(2), 197–211 (2005)
44. Alonso, F.J., Castillo, J.M., Pintado, P.: Application of singular spectrum analysis to the smoothing of raw kinematic signals. J. Biomech. **38**(5), 1085–1092 (2005)
45. Leardini, A., Chiari, L., Croce, U.D., Cappozzo, A.: Human movement analysis using stereophotogrammetry: Part 3. Soft tissue artifact assessment and compensation. Gait Posture **21**(2), 212–225 (2005)
46. Della Croce, U., Leardini, A., Chiari, L., Cappozzo, A.: Human movement analysis using stereophotogrammetry: Part 4: assessment of anatomical landmark misplacement and its effects on joint kinematics. Gait Posture **21**(2), 226–237 (2005)
47. Begon, M., Monnet, T., Lacouture, P.: Effects of movement for estimating the hip joint centre. Gait Posture **25**(3), 353–359 (2007)
48. Lu, T.W., O'Connor, J.J.: Bone position estimation from skin marker co-ordinates using global optimisation with joint constraints. J. Biomech. **32**(2), 129–134 (1999)
49. Begon, M., Wieber, P.B., Yeadon, M.R.: Kinematics estimation of straddled movements on high bar from a limited number of skin markers using a chain model. J. Biomech. **41**(3), 581–586 (2008)
50. Challis, J.H.: A procedure for determining rigid body transformation parameters. J. Biomech. **28**(6), 733–737 (1995)
51. Chèze, L., Fregly, B.J., Dimnet, J.: A solidification procedure to facilitate kinematic analyses based on video system data. J. Biomech. **28**(7), 879–884 (1995)
52. Rao, G., Amarantini, D., Berton, E., Favier, D.: Influence of body segments' parameters estimation models on inverse dynamics solutions during gait. J. Biomech. **39**(8), 1531–1536 (2006)
53. Yeadon, M.R.: The simulation of aerial movement II: A mathematical inertia model of the human body. J. Biomech. **23**(1), 67–74 (1990)
54. Winter, D.A.: Biomechanics and Motor Control of Human Movement. Wiley, New York (1990)
55. Zatsiorsky, V.M., Seluyanov, V., Chugunova, L.: In Vivo Body Segment Inertial Parameters Determination Using a Gamma-Scanner Method. Biomechanics of Human Movement: Applications in Rehabilitation, Sports and Ergonomics. Bertec Corporation, Worthington (1990)

56. de Leva, P.: Adjustments to Zatsiorsky–Seluyanov's segment inertia parameters. J. Biomech. **29**(9), 1223–1230 (1996)
57. Cheng, C.K., Chen, H.H., Chen, C.S., Lee, C.L., Chen, C.Y.: Segment inertial properties of Chinese adults determined from magnetic resonance imaging. Clin. Biomech. **15**(8), 559–566 (2000)
58. Samin, J.-C., Fisette, P.: Symbolic Modeling of Multibody Systems. Kluwer Academic, Dordrecht (2003)
59. Chenut, X., Fisette, P., Samin, J.C.: Recursive formalism with a minimal dynamic parameterization for the identification and simulation of multibody systems. Application to the human body. Multibody Syst. Dyn. **8**(2), 117–140 (2002)
60. Docquier, N., Poncelet, A., Fisette, P.: ROBOTRAN: a powerful symbolic generator of multibody models. Mech. Sci. **4**(1), 199–219 (2013)
61. Fisette, P., Postiau, T., Sass, L., Samin, J.C.: Fully symbolic generation of complex multibody models*. Mech. Struct. Mach. **30**(1), 31–82 (2002)
62. Samin, J.C., Brüls, O., Collard, J.F., Sass, L., Fisette, P.: Multiphysics modeling and optimization of mechatronic multibody systems. Multibody Syst. Dyn. **18**(3), 345–373 (2007)
63. Hof, A.L.: Scaling gait data to body size. Gait Posture **4**(3), 222–223 (1996)
64. Ausejo, S., Suescun, Á., Celigüeta, J.: An optimization method for overdetermined kinematic problems formulated with natural coordinates. Multibody Syst. Dyn. **26**(4), 397–410 (2011)
65. Fohanno, V., Begon, M., Lacouture, P., Colloud, F.: Estimating joint kinematics of a whole body chain model with closed-loop constraints. Multibody Syst. Dyn., 1–17 (2013)
66. Schmidt, R., Disselhorst-Klug, C., Silny, J., Rau, G.: A marker-based measurement procedure for unconstrained wrist and elbow motions. J. Biomech. **32**(6), 615–621 (1999)
67. Hamming, D., Braman, J.P., Phadke, V., LaPrade, R.F., Ludewig, P.M.: The accuracy of measuring glenohumeral motion with a surface humeral cuff. J. Biomech. **45**(7), 1161–1168 (2012)